EUROPEAN JOURNAL OF PURE AND APPLIED MATHEMATICS
2025, Vol. 18, Issue 4, Article Number 6181
ISSN 1307-5543 – ejpam.com
Published by New York Business Global

Numerical Simulation of Cutting Transport in a Drilling Operation by Using TVD RKDG Scheme with WENO Limiters

Ilyas Khan[1,5,6], Asad Rehman[2,*], Shahid Mehmood[3], Saqib Zia[3,*], Wei Sin Koh[4]

[1] *Department of Mathematical Sciences, Saveetha School of Engineering, SIMATS, Chennai, Tamil Nadu, India*
[2] *Department of Information Technology, Pothohar Campus Gujar Khan, University of Punjab, Pakistan*
[3] *Department of Mathematics, COMSATS University Islamabad, Park Road Chak Shehzad, Islamabad, Pakistan*
[4] *INTI International University, Persiaran Perdana BBN Putra Nilai, 71800 Nilai, Negeri Sembilan, Malaysia*
[5] *Hourani Center for Applied Scientific Research, Al-Ahliyya Amman University, Amman, Jordan*
[6] *Department of Mathematics, College of Science Al-Zulfi, Majmaah University, Al-Majmaah 11952, Saudi Arabia*

Abstract. In this article, we present a numerical investigation of two-phase flow involving liquid and solid particles (cuttings) during drilling operations in wellbores. The dynamics of this complex system are simulated using a high-resolution second-order Total Variation Diminishing (TVD) Runge-Kutta Discontinuous Galerkin (RKDG) method, enhanced with a Weighted Essentially Non-Oscillatory (WENO) limiter. Unlike traditional slope-limiter techniques, the integration of WENO methodology with the RKDG scheme significantly improves the accuracy and stability of the numerical solution by effectively capturing sharp interfaces and discontinuities without spurious oscillations. A two-phase drift-flux model is employed to account for the relative motion between the liquid and solid phases, enabling realistic simulation of the transient and dynamic behavior of cuttings transport under various well conditions. Through a series of test cases, we analyze the influence of varying rates of penetration (ROP) on critical parameters such as bottom hole pressure (BHP), cuttings concentration, and pressure evolution over time. The results demonstrate that the proposed scheme offers enhanced accuracy and computational efficiency compared to conventional approaches.

2020 Mathematics Subject Classifications: 65Nxx, 65M08, 65Z05

*Corresponding author.
*Corresponding author.
DOI: https://doi.org/10.29020/nybg.ejpam.v18i4.6181

Email addresses: i.said@mu.edu.sa (I. Khan), assad013@gmail.com (A. Rehman), sm0694921@gmail.com (S. Mehmood), saqibzia81@hotmail.com (S. Zia), weisin.koh@newinti.edu.my (W. S. Koh)

Key Words and Phrases: Two phase flow, rkdg, drift flux flow model, shock wave, source terms, smart microgrids

1. Introduction

The transportation of cuttings in wells has been the subject of experimental investigation by numerous scientist since the second last decade of 20^{th} centuary. Tomren et al. [1] were among the pioneering researchers to study cuttings transport in directional wells. The extraction of drill cuttings from the bore-hole is a pivotal step during drilling operations, especially when working on horizontal, extended-reach, or slanting wells. Lack of proper bore-hole cleaning can result in substantial issues, such as pipe obstructions, reduced drilling velocity, increased bit wear, fluid loss, and excessive torque and drag. A well-designed drilling mud and an appropriate circulation system are essential for ensuring the extraction of cuttings from the bore-hole. The success of the drilling operation is greatly impacted by a number of critical elements, such as the type of formation, wellbore inclination, cutting size, penetration rate, and eccentricity of the drill pipe. It is difficult to create an ideal hole cleaning plan that considers each of these aspects [2–5].

Two phase flow models are critical for predicting fluid behaviours in many different industrial applications, including power production, cooling systems, and the extraction of gas and oil. These models hold significant value for multiple objectives, including gaining insights into fluid dynamics within pipelines, heat exchangers, and other machinery; facilitating the design and optimization of industrial processes; improving efficiency and reducing operational costs; and mitigating safety threats such as leaks and explosions[6–8].

To explore the attributes of two phase flows, scientists have devised various models and an extensive array of numerical methods. However, regardless of significance, these models can pose numerical challenges because of the complexities arising from the interface between the both phases. Specifically, these models present various numerical obstacles, such as discontinuous solutions, shock formation, and loss of hyperbolicity. To address these numerical challenges, drift flux model was introduced by Zuber and Findly [9]. Subsequently, several authors have made improvements and modifications to the drift flux flow model, as demonstrated in articles [10–14]. In transient-state and steady-state models the primary distinction is lies in the representation of the equations of motion. The rate of change of velocity, density and temperature involve in the transient equations of motion. A pipeline flow is typically characterized as a transient process due to the changing inlet and outlet flows. Moreover, variations in ambient conditions, control set points, and temperature further contribute to this transient behavior. Therefore, having a transient flow model that accurately captures the dynamics occurring in the system proves advantageous [15].

In this article, RKDG is developed to simulate the cuttings flow in well operations by considering the two phase drift flux model. This method combines the best features of finite element methods (such as weak formulation and test function spaces) and finite volume methods (such as nonlinear limiters, numerical fluxes and smart microgrids). First

of all, the discontinuous Galerkin numerical method was developed by Reed and Hill [16] to solve the hyperbolic equations. After that this numerical scheme was extended and employed to solve parabolic, elliptic and hyperbolic types of partial differential equations [17–19]. This scheme was further modified by Cockburn and his team in [20–23]. The explicit time discretization techniques for total variation diminishing (TVD) were discussed in [24–27]. The proposed numerical scheme maintains the property of total variation bounded in the means. This scheme is capable to handle sharp shock transitions, without introducing oscillations. Further, the artificial viscosity is introduced by the numerical flux through upwinding to maintain stability in the scheme when employing piecewise-constant approximations, for detail see [20, 21, 24, 25].

This work presents a refined numerical approach for simulating two-phase drilling hydraulics by coupling the Runge-Kutta Discontinuous Galerkin (RKDG) method with WENO limiters within a drift-flux framework.To the best of our knowledge, only the Advection Upstream Splitting Method – Velocity (AUSMV) numerical scheme has been employed previously to simulate cuttings transport in well operations [28]. The incorporation of WENO limiters [29–32] into the time-stepping algorithm enhances stability and effectively suppresses spurious oscillations. The resulting scheme accurately resolves shock phenomena and maintains sharp solution profiles with high fidelity. Through various test cases, the influence of changing rates of penetration (ROP) on bottom hole pressure (BHP), cuttings concentration, and pressure evolution is systematically analyzed. The results confirm that the proposed method outperforms conventional schemes in both accuracy and computational efficiency. Future studies may focus on extending the current model to incorporate non-Newtonian fluid effects and thermal variations, which are critical in real-world drilling environments. Additionally, the proposed numerical scheme can be extended to compute the solutions of nonlinear partial differential equations such as [33–36].

The rest of article is structured as follows. In section 2, the mathematical form of two phase drift flux model and eigen structure is presented. In section 3, the TVD RKDG is derived for the proposed mode. In section 4, different cases are considered to analyze the effects of cuttings on bottom hole pressure and observe the effects of different parameters in the process of cutting flows. Finally, the conclusions are drawn in section 5.

2. Drift flux model for two phase flows

In this section, we present the mathematical representation of the two phase drift flux model [9] and provide an explanation of its eigenvalues. The model is based on several key assumptions to simplify the complex physics of multiphase transport. Firstly, both the liquid and solid phases are assumed to share a common pressure field. Assuming that the cuttings are sufficiently small and uniformly distributed. The relative motion between phases is captured using empirical drift velocity correlations. Additionally, the model assumes isothermal conditions and neglects thermal effects on fluid or particle behavior. Drift flux model consists of three partial differential equation, two of them are liquid and cutting phase mass conservation equations and one mixture momentum equations are

given here

$$\begin{aligned}
&\frac{\partial}{\partial_t}(a_l\rho_l) + \frac{\partial}{\partial_x}(a_l\rho_l u_l) = 0,\\
&\frac{\partial}{\partial_t}(a_g\rho_g) + \frac{\partial}{\partial_x}(a_g\rho_g u_g) = 0,\\
&\frac{\partial}{\partial_t}(a_l\rho_l u_l + a_g\rho_g u_g) + \frac{\partial}{\partial_x}(a_l\rho_l u_l^2 + a_g\rho_g u_g^2 + p) = s,
\end{aligned} \tag{1}$$

where a_g and a_l represent the volume fractions of cutting and liquid, u_g and u_l denote the cutting and liquid velocities, ρ_g and ρ_l represent cutting and liquid densities, respectively. The cuttings density was assumed fixed to be $2500kg/m^3$. The source term is denoted by s. The mutual pressure is represented by p .

$$s = F_f + G_f = -\frac{32u_{mix}\mu_{mix}}{\mathcal{D}^2} + (a_g\rho_g + a_l\rho_l)g, \tag{2}$$

The diameter of pipeline from the inner side is denoted by $\mathcal{D}$ and $g = 9.81\ m/s^2$. Viscosity term μ_{mix} and the average velocity term u_{mix} in the frictional forces F_f are

$$\mu_{mix} = a_l\mu_l + a_g\mu_g \quad \text{and} \quad u_{mix} = a_g u_g + a_l u_l. \tag{3}$$

There are seven unknown variables are involved in drift flux model $a_l, a_g,\ \rho_l, \rho_g,\ u_l, u_g,$ and p. Consequently, to obtain a solution, it is necessary to establish four additional relationships, which are as follows:

$$\rho_l = \rho_{l,0} + \frac{p - p_{l,0}}{\alpha_l^2}, \tag{4}$$

The pressure is calculated by the following relation

$$p = p_{l,0} + \left(\frac{a_l\rho_l}{(1-a_g)} - \rho_{l,0}\right)\cdot a_l^2, \tag{5}$$

$$a_l + a_g = 1. \tag{6}$$

and

$$u_g = C_o u_{mix} + u_d, \tag{7}$$

here,α_l represent the speed of sound in liquid phase. Additionally, $\rho_{l,0}$ and $p_{l,0}$ are the reference liquid density and reference liquid pressure, while C_o and u_d represent the drift cutting velocity and a flow-dependent parameter. The specific values for these parameters are given in Table 1.

2.1. Eigenvalues calculation

The drift flux model (1) is represented in the conservation laws form

$$\partial_t\mathbf{W} + \partial_x\mathbf{F}(\mathbf{W}) = \mathbf{S}(\mathbf{W}), \tag{8}$$

where

Table 1: Parameter values.

Description	**Parameters**	**Value**
cutting phase viscosity	μ_g	$2.10^{-2}\ Pa.s$
liquid phase viscosity	μ_l	$5.10^{-2}\ Pa.s$
velocity of sound in cutting phase	α_g	$1500\ m/second$
velocity of sound in liquid phase	α_l	$1000\ m/second$
reference density liquid	$\rho_{l,0}$	$1000\ Kg/m^3$
reference pressure liquid	$p_{l,0}$	$10^5\ Pa$
choke pressure	p_{choke}	100 bars

$$\mathbf{W} = \begin{pmatrix} a_l\rho_l \\ a_g\rho_g \\ a_l\rho_l u_l + a_g\rho_g u_g \end{pmatrix}, \quad \mathbf{F}(\mathbf{W}) = \begin{pmatrix} a_l\rho_l u_l \\ a_g\rho_g u_g \\ a_l\rho_l u_l^2 + a_g\rho_g u_g^2 + p \end{pmatrix}, \mathbf{S}(\mathbf{W}) = \begin{pmatrix} 0 \\ 0 \\ s \end{pmatrix},$$

with, $\mathbf{S}(\mathbf{W}) = (s_1, s_2, s_3) = (0, 0, s)$, $\mathbf{F}(\mathbf{W}) = (f_1,\ f_2,\ f_3) = (a_l\rho_l u_l,\ a_g\rho_g u_g, a_l\rho_l u_l^2 + a_g\rho_g u_g^2 + p)$ and $\mathbf{W} = (w_1,\ w_2,\ w_3) = (a_l\rho_l,\ a_g\rho_g,\ a_l\rho_l u_l + a_g\rho_g u_g)$. Now, the Eq. (8) can be expressed as

$$\partial_t \begin{pmatrix} w_1 \\ w_2 \\ w_3 \end{pmatrix} + \partial_x \begin{pmatrix} w_1 w_l \\ w_2 w_g \\ w_1 w_l^2 + w_2 w_g^2 + p(w_1, w_2) \end{pmatrix} = \begin{pmatrix} 0 \\ 0 \\ s \end{pmatrix}. \tag{9}$$

We have observed that the entire flux vector cannot be entirely expressed using the conserved variables in this system, making it impossible to precisely determine the sound velocity. The papers [37, 38] provide comprehensive explanations for approximation of the sound velocity. Although we have omitted the procedural details here, we will only consider the eigenvalues. Eigenvalues for the considered model is,

$$\begin{aligned} \lambda_1 &= u - \alpha, \\ \lambda_2 &= u, \\ \lambda_3 &= u + \alpha. \end{aligned} \tag{10}$$

Where,

$$\alpha = \sqrt{\frac{p}{a_g\rho_l(1 - C_o a_g)}}. \tag{11}$$

3. Construction of TVD RKDG scheme for the drift flux model

In this section, we obtain the two phase drift flux flow model using the RKDG scheme. This model is written in compact form as

$$\partial_t \mathbf{W} + \partial_x \mathbf{F}(\mathbf{W}) = \mathbf{S}(\mathbf{W}), \quad t > 0, x \in \Omega. \tag{12}$$

with initial conditions

$$\mathbf{W}(x,0) = \mathbf{W}_0(x). \tag{13}$$

We subdivide the domain Ω into cells $C_i = [x_{i-\frac{1}{2}}, x_{i+\frac{1}{2}}]$, where $i = 1, ..., N$. We denote the center of i_{th} cell by x_i and defined as $0.5\left(x_{i-\frac{1}{2}} + x_{i+\frac{1}{2}}\right)$. The size of i_{th} cell is defined as $\triangle x_i = x_{i+\frac{1}{2}} - x_{i-\frac{1}{2}}$, for all i. Multiply the Eq. (12) by a smooth function $\tau(x)$ and integrate the resulting equation over the i_{th} cell C_i. By integrating, we obtain

$$\begin{aligned}&\int_{C_i} \partial_t \mathbf{W}(x,t)\tau(x)dx - \int_{C_i} \mathbf{F}(\mathbf{W}(x,t))\partial_x\tau(x)dx \\ &+ \mathbf{F}(\mathbf{W}(x_{i+\frac{1}{2}},t))\tau(x_{i+\frac{1}{2}}) - \mathbf{F}(\mathbf{W}(x_{i-\frac{1}{2}},t))\tau(x_{i-\frac{1}{2}}) = \int_{C_i} \mathbf{S}(\mathbf{W}(x,t))\partial_x\tau(x)dx,\end{aligned} \tag{14}$$

and

$$\int_{C_i} \mathbf{W}(x,0)\tau(x)dx = \int_{C_i} \mathbf{W}_0(x)\tau(x)dx. \tag{15}$$

Consider for each time $t \in [0, t_{final}]$, the solution approximation $\mathbf{W}_h$ of $\mathbf{W}$ belongs to discontinuous Galerkin finite element space

$$\mathcal{V}_h = \{\upsilon : \upsilon|_{C_i} \in \mathcal{P}^k(C_i), i = 0, 1, 2...N\}. \tag{16}$$

The $\mathcal{P}^k(C_i)$ is the polynomials space of degree at most k in cell C_i. We choose the local orthogonal basis $\{\varphi_i^l, l = 0, 1, 2, ..., k\}$, named as scaled Legendre polynomials $\mathcal{P}_l(x)$, over cell C_i as defined below

$$\varphi_i^l(x) = \mathcal{P}_l((x - x_i)/\triangle x_i), \quad l = 0, 1, 2, ...k. \tag{17}$$

Then, the approximate solution $\mathbf{W}_h(x,t) \in \mathcal{V}_h$ is defined as

$$\mathbf{W}_h(x,t) = \sum_{l=0}^{k} \mathbf{W}_i^l(t)\varphi_i^l(x), \quad \text{for} \quad x \in C_i, \tag{18}$$

where, $\mathbf{W}_i^l(t) = \frac{2l+1}{\triangle x_i}\int_{C_i} \mathbf{W}_h(x,t)\varphi_i^l(x)dx$ by using the orthogonal property

$$\int_{C_i} \varphi_i^l \varphi_i^m dx = \begin{cases} 0, & l \neq m \\ \frac{\triangle x_i}{2l+1}, & l = m. \end{cases}$$

Now, replace a smooth function $\tau(x)$ by the test function $\varphi_l(x) \in \mathcal{V}_h$ and flux function $\mathbf{F}(\mathbf{W}(x_{i+\frac{1}{2}},t))$ by numerical flux $\hat{\mathbf{F}}_{i+\frac{1}{2}}$ in Eqs. (14) and (15) to obtain a numerical scheme as follow

$$\int_{C_i} \partial_t \mathbf{W}_h(x,t)\varphi_l(x)dx - \int_{C_i} \mathbf{F}(\mathbf{W}_h(x,t))\partial_x\varphi_l(x)dx + \hat{\mathbf{F}}_{i+\frac{1}{2}}\varphi_l(x^-_{i+\frac{1}{2}}) - \hat{\mathbf{F}}_{i-\frac{1}{2}}\varphi_l(x^+_{i-\frac{1}{2}}) =$$

$$\int_{C_i} \mathbf{S}(\mathbf{W}_h(x,t))\varphi_l(x)dx, \tag{19}$$

with

$$\int_{C_i} \mathbf{W}_h(x,0)\varphi_l(x)dx = \int_{C_i} \mathbf{W}_0(x)\varphi_l(x)dx. \tag{20}$$

The flux $\hat{F}_{i+\frac{1}{2}} = \digamma\left(\mathbf{W}_h(x^-_{i+\frac{1}{2}},t), \mathbf{W}_h(x^+_{i+\frac{1}{2}},t)\right)$ is any monotone numerical flux. Here, we use the Local Lax-Friedrichs as a monotone numerical flux which is defined below

$$\digamma\left(\mathbf{W}^-_{i+\frac{1}{2}}, \mathbf{W}^+_{i+\frac{1}{2}}\right) = \frac{1}{2}\left(\mathbf{F}(\mathbf{W}^-_{i+\frac{1}{2}}) + \mathbf{F}(\mathbf{W}^+_{i+\frac{1}{2}}) - \vartheta(\mathbf{W}^+_{i+\frac{1}{2}} - \mathbf{W}^-_{i+\frac{1}{2}})\right), \tag{21}$$

where $\vartheta = \max_W |\mathbf{F}'(\mathbf{W})|$ and $\mathbf{W}_h(x^{\pm}_{i+\frac{1}{2}},t)$ are the limited values of approximate solution $\mathbf{W}_h(x,t)$ at the cell interface $x_{i+\frac{1}{2}}$. By using above definitions, the Eqs. (19) and (20) simplify to

$$\frac{d\mathbf{W}^l_i(t)}{dt} = -\frac{2l+1}{\triangle x_i}\left(\int_{C_i} \mathbf{F}(\mathbf{W}_h(x,t))\partial_x\varphi_l(x)dx + \hat{\mathbf{F}}_{i+\frac{1}{2}}\varphi_l(x^-_{i+\frac{1}{2}}) - \hat{\mathbf{F}}_{i-\frac{1}{2}}\varphi_l(x^+_{i-\frac{1}{2}}) + \int_{C_i} \mathbf{S}(\mathbf{W}_h(x,t))\varphi_l(x)dx\right), \tag{22}$$

and

$$\mathbf{W}^l_i(0) = \frac{2l+1}{\triangle x_i}\int_{C_i} \mathbf{W}_0(x)\varphi^l_i(x)dx. \tag{23}$$

Next, to obtain non-oscillatory discontinuity propagation and high order accuracy by RKDG method, the limiter procedure is divided into two parts. Firstly, identify the cells, named as "troubled cells", that may need the limiting procedure. Secondly, reconstruct the polynomial solutions in these troubled cells by using WENO reconstruction.
Here, the troubled cells are identified by total variation bounded (TVB) limiter [39], which is described as

$$\mathbf{W}_h(x^+_{i+\frac{1}{2}}) = \mathbf{W}^{(0)}_i + \overline{\mathbf{W}}_i, \quad \mathbf{W}_h(x^+_{i-\frac{1}{2}}) = \mathbf{W}^{(0)}_i - \overline{\overline{\mathbf{W}}}_i, \tag{24}$$

where

$$\overline{\mathbf{W}}_i = \sum_{l=1}^{k} \mathbf{W}^l_i\varphi^l(x_{i+\frac{1}{2}}), \quad \overline{\overline{\mathbf{W}}}_i = -\sum_{l=1}^{k} \mathbf{W}^l_i\varphi^l(x_{i-\frac{1}{2}}).$$

Now $\overline{\mathbf{W}}_i$ and $\overline{\overline{\mathbf{W}}}_i$ are modified by the modified minmod (MM) function, as follow

$$\overline{\mathbf{W}}^{mod}_i = \mathsf{MM}(\overline{\mathbf{W}}_i, \mathbf{W}^{(0)}_{i+1} - \mathbf{W}^{(0)}_i,\ \mathbf{W}^{(0)}_i - \mathbf{W}^{(0)}_{i-1}),$$

$$\overline{\overline{\mathbf{W}}}_i^{mod} = \mathsf{MM}(\overline{\overline{\mathbf{W}}}_i, \mathbf{W}_{i+1}^{(0)} - \mathbf{W}_i^{(0)},\ \mathbf{W}_i^{(0)} - \mathbf{W}_{i-1}^{(0)}),$$

where MM is defined as

$$\mathsf{MM}(a_1, a_2, a_3) = \begin{cases} a_1, & \text{if } |a_1| \leq M(\triangle x)^2, \\ \mathsf{M}(a_1, a_2, a_3), & \text{otherwise,} \end{cases}$$

where M is a positive constant and the minmod function M is defined as

$$\mathsf{M}(a_1, a_2, a_3) = \begin{cases} S \cdot \min_{1\leq i\leq n} |a_i|, & \text{if } \operatorname{sign}(a_1) = \operatorname{sign}(a_2) = \operatorname{sign}(a_3) = S, \\ 0, & \text{otherwise.} \end{cases}$$

Note that, the cell C_i is called a troubled cell when $\overline{\mathbf{W}}_i^{mod} \neq \overline{\mathbf{W}}_i$ and $\overline{\overline{\mathbf{W}}}_i^{mod} \neq \overline{\overline{\mathbf{W}}}_i$. For the troubled cell, the moments $\mathbf{W}_i^l$ are reconstructed by the WENO reconstruction which retains the cell average $\mathbf{W}_i^{(0)}$. Note that, for the $(k+1)$-th order accurate $\mathcal{P}^k$ based DG scheme, we use the Gauss Lobatto quadrature rule which is accurate at least up to the order $(2k+2)$ and the order of accuracy for the WENO reconstruction must be at least $(2k+1)$. To achieve this, $(2k+1)$ neighboring cells $C_{i-k}, ..., C_{i+k}$ are used for reconstruction of the point values of $\mathbf{W}$ at the Gauss Lobatto quadrature points. Next, for the reconstruction of WENO limiter for RKDG scheme, we will follow the same approach as described in [30] and obtained the WENO approximation to the moments as follows

$$\mathbf{W}_i^l = \frac{2l+1}{\triangle x_i} \sum_{m=0}^{k} \omega_m \int_{C_i} p_m(x) \varphi_i^l(x) dx \quad l = 1, ..., k. \tag{25}$$

Here, $p_m(x)$ denotes the k-th degree reconstructed polynomial associated with each of the stencils $\tau_m = \cup_{l=0}^{k} C_{i+m-l}, \quad m = 0, ..., k$ and ω_m are the nonlinear weights defined as

$$\omega_m = \frac{\overline{\omega}_m}{\sum_m \overline{\omega}_m}, \quad \overline{\omega}_m = \frac{\gamma_m}{(\varepsilon + \mathfrak{B}_m)^2}, \tag{26}$$

where $\mathfrak{B}_m$ is the smooth indicator for each cell C_i which measure the smoothness of function $p_m(x)$ in the cell C_i. The $\mathfrak{B}_m$ is defined as follow

$$\mathfrak{B}_m = \sum_m \int_{C_i} \triangle x_i^{2l-1} \left(\frac{\partial^l}{\partial x^l} p_m(x) \right)^2 dx. \tag{27}$$

The remaining two terms γ_m and ε in Eq. (26) respectively denote the linear weights and small constant which is usually taken as 10^-6. Further, the linear weights γ_m should satisfy the following relation

$$\int_{C_i} q(x) \varphi_i^l(x) dx = \sum_{m=0}^{k} \gamma_m \int_{C_i} p_m(x) \varphi_i^l(x) dx, \quad l = 1, ..., k, \tag{28}$$

where $q(x)$ denotes the $2k$-th degree reconstructed polynomial, associated with the larger stencil $\mathcal{T} = \cup_{m=0}^{k} \tau_m$ [29]. For time discretization, we will use second order TVD Runge-Kutta method [40]. The system of ordinary differential equations (22) can be written in the compact form as follows,

$$\frac{d\mathbf{W}_h}{dt} = L_h(t, \mathbf{W}_h)\,. \tag{29}$$

To approximate equation (29), one may used r-order TVD RK,

$$\mathbf{W}_h^{(k)} = \sum_{l=0}^{k-1} \left[\alpha_{kl}\mathbf{W}_h^{(l)} + \beta_{kl}\Delta t L_h(t^n + d_l\Delta t, \mathbf{W}_h^{(l)})\right], \quad k = 1, 2, \cdots, r\,, \tag{30}$$

by using the boundary conditions

$$\mathbf{W}_h^{(0)} = \mathbf{W}_h^n\,, \quad \mathbf{W}_h^{(r)} = \mathbf{W}_h^{n+1}\,. \tag{31}$$

The coefficients for the second-order TVD RKM are provided as follows:[20]

$$\beta_{10} = \alpha_{10} = 1\,, \quad \beta_{21} = \alpha_{20} = \alpha_{21} = \frac{1}{2}\,, \quad d_0 = 0\,, \quad d_1 = 1, \quad \beta_{20} = 0. \tag{32}$$

While, the coefficients for the third-order TVD RK are provided as follows

$$\begin{aligned}\beta_{10} =&\alpha_{10} = 1\,, \quad \beta_{20} = 0\,, \quad \alpha_{20} = \frac{3}{4}\,, \quad \beta_{21} = \alpha_{21} = \frac{1}{4}\,, \quad \alpha_{30} = \frac{1}{3}\,,\\ &\beta_{31} = \beta_{30} = \alpha_{31} = 0\,, \quad \beta_{32} = \alpha_{32} = \frac{2}{3}\,, \quad d_2 = \frac{1}{2}\,, \quad d_1 = 1\,, \quad d_0 = 0\,.\end{aligned} \tag{33}$$

The following condition

$$\Delta t \leq \left(\frac{1}{2k+1}\right)\frac{\min(\Delta x_j)}{\lambda_{max}}\,, \tag{34}$$

is known as Courant-Friedrichs-Lewy (CFL) condition [20], where Δt, k, Δx_j, $\min(\Delta x_j)$ and λ_{max} represent time step, degree of polynomial used in DG scheme, spacial cell size, the most restrictive condition over the grid and maximum speed. The CFL condition is used in the time step scheme for ensuring the stability and convergence of the numerical scheme.

Here, $k = 1, 2$ is the order of scheme which is second and third order respectively, and λ_{max} reprsents the maximum eigenvalue. The adaptive nature of this time step results in a decrease for scenarios involving substantial variations (large slopes) in the solution and an increase otherwise.

4. Numerical Simulation

In this section, five different test cases [28] are considered to analyze the efficiency of and proposed numerical scheme.More precisely, the proposed numerical scheme is used to examine the influence of cuttings on bottom-hole pressure, observes the variations of BHP over time, and explores the impact of changing penetration rates on BHP throughout the time duration. We consider the consistent geometry across all given cases, the depth of well is taken as 2000 m and inner diameter of the well is 5 inches, while the outer diameter is 8.5 inches. For complete description, the reader is referred to [28].

Case 1: A no-slip model is considered in the this case and over various time intervals the changes in cutting concentrations are observed. Before pumping starts, the well is completely full with liquid, and the flow rates are 22 kg/s with a cutting flux of 2 kg/s at the bottom of the well. In Figure 1, at 500 s, it is evident that well lower part contains cuttings, indicating the transportation of cuttings out of the well. However, initially, the cutting concentration is zero up to a depth of 1250 m, and then it steadily increases, eventually approaching a value of 0.04, as shown in the figure. Moving on to Figure 2, the cutting has progressed higher up in the well at 1500 s. It is also observed that the concentration values are constant, indicating a stable state, specifically from 1400 m to 2000 m. In contrast to Figures 1 and 2, Figure 3 shows that the steady state of the cutting concentration is achieved at a shorter well depth at a depth of 2000 m. Constantly cutting concentration values are observed from a depth of 1150 m onward. After 3000 s, the steady state is reached in Figure 4, and the cutting concentrations are consistently seen over the whole well. Figure 5 displays the final steady state conditions when the final time is set to 4000 s. The cutting concentration is measured at 0.04, indicating that the cuttings are distributed throughout the entire well. Figure 6 shows a graph of bottom hole Pressure over time in the well, highlighting how the cutting rate impacts BHP. When we first begin pumping cuttings into the well, it takes around 200 s for BHP to start rising. This rise is due to the friction within the well caused by the start of the flow rate. As the well continues to fill with cuttings, the BHP steadily increases.

Case 2: In this case, we introduce a change in the mass rate of cutting, which is now

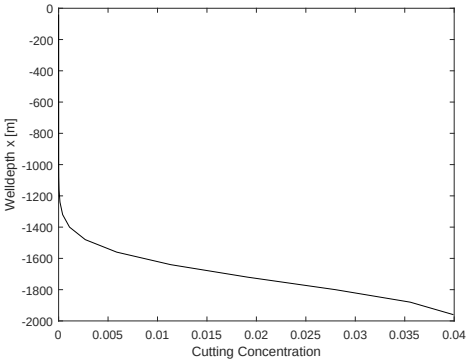

Figure 1: Case 1: t= 500 s, mass rate = 2 kg/s, plotting of well depth vs cuttings concentration.

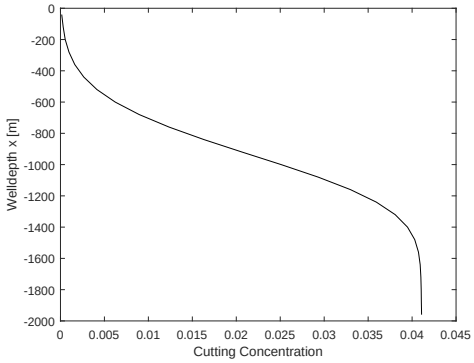

Figure 2: Case 1: $t = 1500$ s, mass rate = 2 kg/s, plotting of well depth vs cuttings concentration.

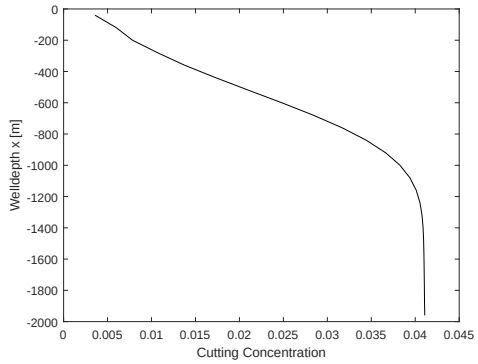

Figure 3: Case 1: t= 2000 s, mass rate = 2 kg/s, plotting of well depth vs cuttings concentration.

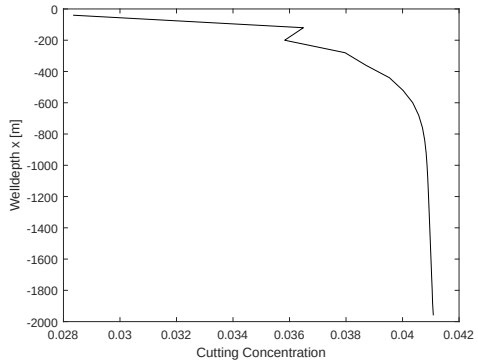

Figure 4: Case 1: t= 3000s, mass rate = 2 kg/s, plotting of well depth vs cuttings concentration.

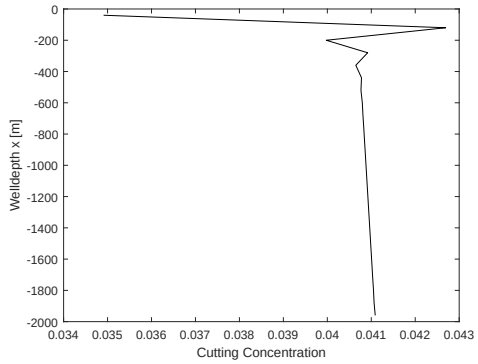

Figure 5: Case 1: t= 4000 s, mass rate = 2 kg/s, plotting of well depth vs cuttings concentration.

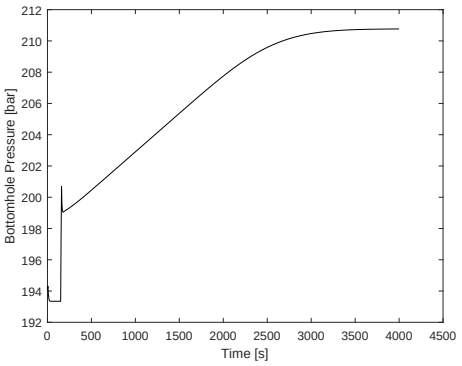

Figure 6: Case 1: t= 4000 s, plotting of bottom hole pressure vs time.

set at 4 kg/s. We observe variations in the concentrations of the cutting for different time intervals, while keeping all other variables the same as in Case 1 . Figure 7 demonstrates that when using a higher cutting rate, the cutting concentrations are also higher, reaching a value of 0.077. This concentration is higher compared to the previous case. Similar to Case 1, the cutting concentrations initially start at zero up to a depth of 1250 m, and then steadily increase, approaching the value of 0.077. In Figure 8, we observe that the concentration of the cutting gradually increases from a depth of 400 m to 1400 m. At a level of 0.77 concentration, it reaches a steady state. This indicates that the cutting is distributed primarily in the lower part of the well. According to Figure 9, the cutting concentration reaches its steady state at a shorter hole depth at 2000 s when compared to Figures 7 and 8. At around 1150 m down, the concentration reaches its steady state. Figure 10 depicts that the cutting concentration can be distributed throughout the entire well relatively quickly. Constant cutting concentrations are observed from a depth of 250 m to 2000 m. At 4000 s, constant cutting concentrations of 0.077 are shown over the whole well in figure 11. The well's bottom hole pressure against time plot is shown in Figure 12, which illustrates how the cutting rate impacts BHP. Like Case 1, an initial

increase in BHP occurs when pumping cuttings and liquid begins, attributed to friction. Gradual increases in BHP are observed due to the hydrostatic pressure as the cuttings are moved upward in the well. It takes around 3500 s to reach a steady condition. When the injection rates are zeroed out at 4000s, well friction goes away. The difference between the simulations in both cases is mainly due to the content of cuttings in the well. The steady state pressure observed during circulation is higher in this case, which can be attributed to the higher cutting rate and resulting higher cutting concentration.

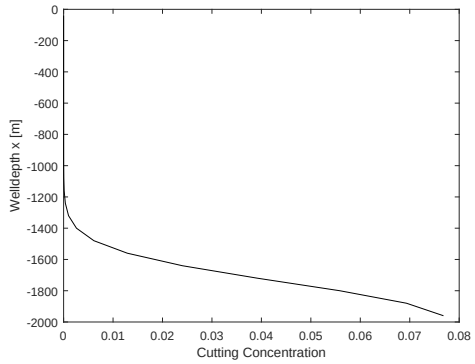

Figure 7: Case 2: t= 500 s, mass rate = 4 kg/s, plotting of well depth vs cuttings concentration.

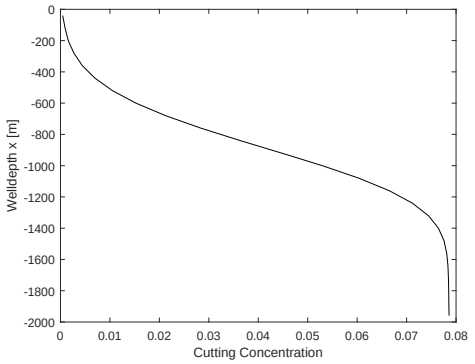

Figure 8: Case 2: t= 1500 s, mass rate = 4 kg/s, plotting of well depth vs cuttings concentration.

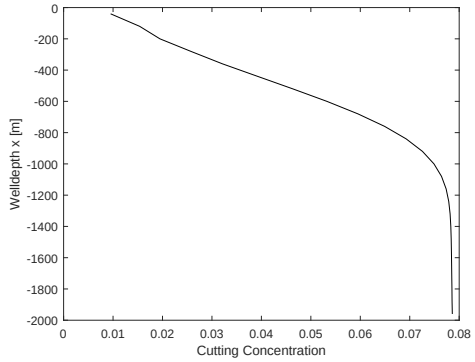

Figure 9: Case 2: t= 2000 s, mass rate = 4 kg/s, plotting of well depth vs cuttings concentration.

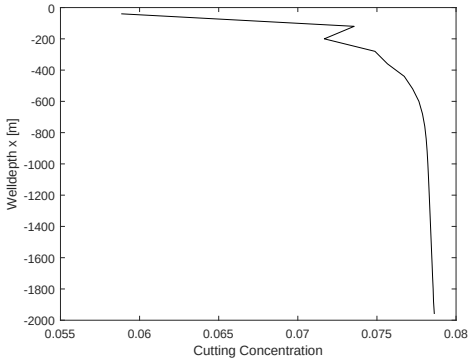

Figure 10: Case 2: t= 3000 s, mass rate = 4 kg/s, plotting of well depth vs cuttings concentration.

Case 3: In this case, we will simulate with a cuttings mass rate of 6 kg/s, while the end times change according to time intervals. The cuttings have penetrated a depth of 1250 m at 500s, as seen in Figure 13. However, as a result of the increased cutting rate of 6 kg/s, the concentration of cuttings is roughly 0.115 at the conclusion of the simulation, which is greater than in the prior situations. In Figure 14, the concentration of the cuttings rises steadily from 400 m to 1400 m, after which it steady state at 0.115, much as in the other instances. This points to the bottom of the well as the primary distribution point for the cuttings. The steady state of the cutting concentration is achieved at a shorter

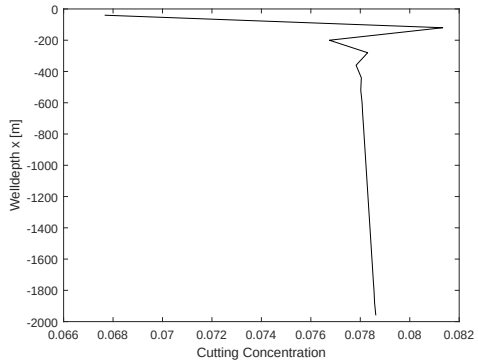

Figure 11: Case 2: t= 4000 s, mass rate = 4 kg/s, plotting of well depth vs cuttings concentration.

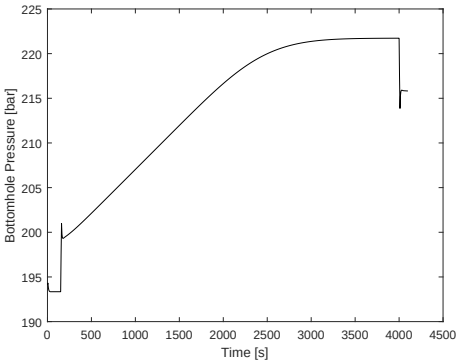

Figure 12: Case 2: t= 4000 s, mass rate = 4 kg/s, plotting of bottom hole pressure vs time.

well depth compared to Figures 13 and 14, as shown in figure 15, when the end time is raised to 2000 s. At around 1150 m down, the concentration reaches its steady state. At 3000 s, as shown in Figure 16, the cuttings have been distributed throughout the entire well. Constant cutting concentrations can be observed from a depth of 250 m to 2000 m. In Figure 17, at 4000 s, the cuttings concentration is the same across the entire well, indicating the achievement of final steady state conditions. From 2 kg/s to 4 kg/s and then 6 kg/s, the cuttings concentration grew in accordance with the cuttings mass rate. In Figure 18, we can see the well's bottomhole Pressure (BHP) plotted against time. As in earlier instances, the first rise in BHP at 200 s is caused by the friction that occurs when cuttings and liquid are pumped. As the cuttings ascend in the well, the hydrostatic pressure rises, and the BHP rises with it. A steady condition is achieved after 3500 s. When the injection rates are turned off after 4000 s, the only pressure that remains is hydrostatic pressure, as well friction goes away. Here, we see stronger pressure than in the prior instances since the cuttings concentration is higher because to the higher cuttings rate.

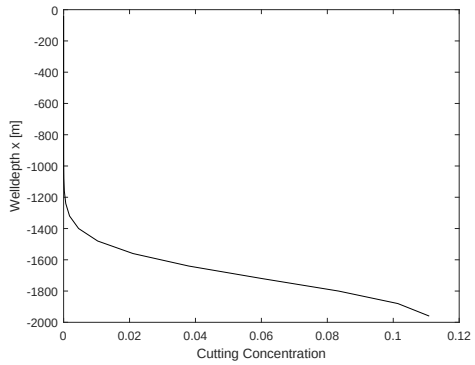

Figure 13: Case 3: t = 500 s, mass rate = 6 kg/s, plotting of well depth vs cuttings concentration.

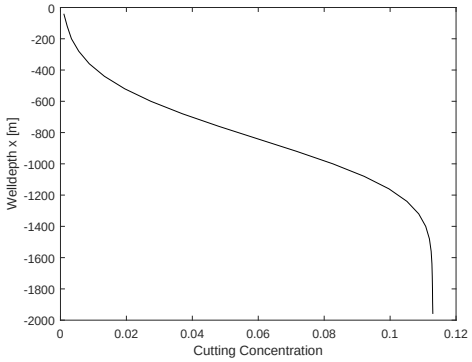

Figure 14: Case 3: t = 1500 s, mass rate = 6 kg/s, plotting of well depth vs cuttings concentration.

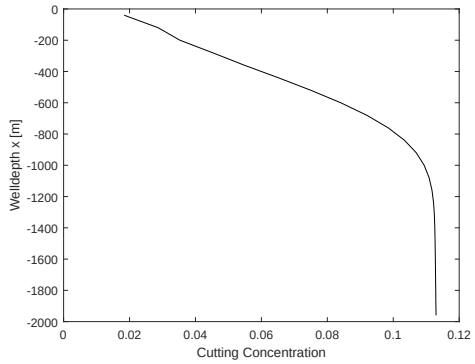

Figure 15: Case 3: t = 2000 s, mass rate = 6 kg/s, plotting of well depth vs cuttings concentration.

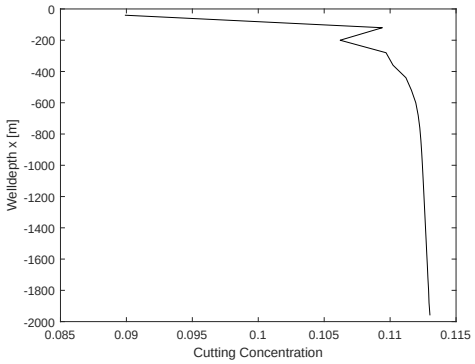

Figure 16: Case 3: t = 3000 s, mass rate = 6 kg/s, plotting of well depth vs cuttings concentration.

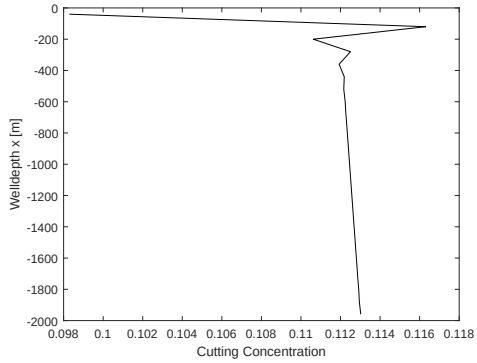

Figure 17: Case 3: t = 4000 s, mass rate = 6 kg/s, plotting of well depth vs cuttings concentration.

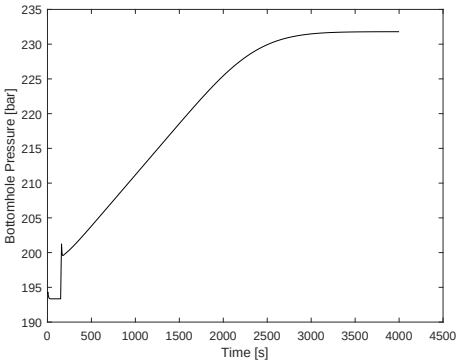

Figure 18: Case 3: t = 4000 s, mass rate = 6 kg/s, plotting of bottom hole pressure vs time.

Case 4: In this test case, we consider two different rate of penetrations: an ROP of 10 m/h and an ROP of 30 m/h, which correspond to mass rates of 0.166 kg/s and 0.498 kg/s, respectively. Figure 19 illustrates that the cutting concentrations increase gradually until reaching a constant value of 3.55×10^{-3}. The cuttings front appears to be smeared out, which can be attributed to numerical diffusion. In Figure 20, we observe that near this constant value, the cutting concentrations remain steady over a time period of 4000 s. At a ROP of 10 m/h, the simulation results are shown in Figure 21. After 200 s of inactivity, the flow rates are activated, leading to a pressure rise caused by friction, after which the well is left static. On the other hand, there is much less cutting buildup since the cutting rate is far smaller. At a ROP of 30 m/h, the simulation results are shown in Figure 22. After 1500 s, you may see cuttings at the well's bottom. At this mass rate, which corresponds to a Rate of Penetration (ROP) of 30 m/h the concentration is more noticeable. The concentration of the cuttings is 0.01 in Figure 23, which is almost three times higher than the concentration of 0.00355 in Figure 20. As the ROP grows, the cutting concentration visibly increases. Higher ROP produces a larger volume of cuttings

in a shorter time, increasing the solid phase concentration in the annular flow. This results in sharper gradients and stronger discontinuities in volume fraction, velocity, and pressure fields.

Figure 24 shows that our ultimate steady-state BHP is 201.9 *bar*, which is higher than the 199.8 *bar* result from the prior simulation. Because of the increased cutting concentration, the BHP has increased. Also, between 2000 s and 4000 s, there is a change in BHP of 2.1 bar (201.9 - 198.8), which is the hydrostatic contribution of the cuttings. Additional research is required to confirm that pressure pulses are the source of the peak at 2000 s. There is a rising tendency in the maximum BHP value, which means that BHP grows as ROP does. This test case demonstrates that the WENO-limited RKDG scheme remains stable even under high rates of penetration (ROP), which typically introduce steep changes in bottom hole pressure (BHP) and cuttings concentration.

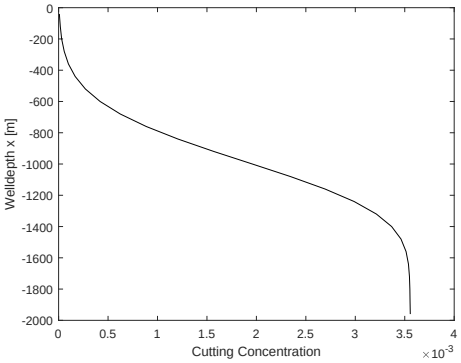

Figure 19: Case 4: t = 1500 s, mass rate = 0.166 kg/s, plotting of well depth vs cuttings concentration.

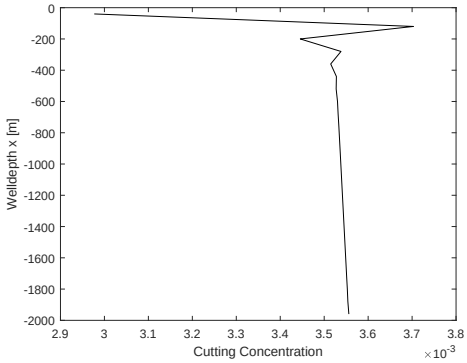

Figure 20: Case 4: t = 4000 s, mass rate = 0.166 kg/s, plotting of well depth vs cuttings concentration.

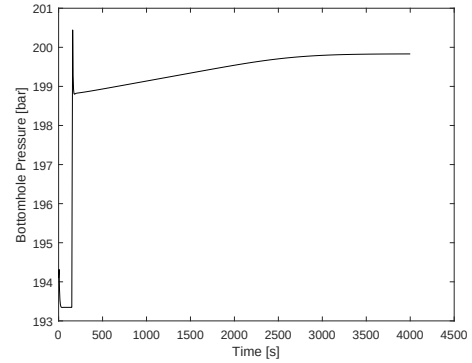

Figure 21: Case 4: t = 4000 s, mass rate = 0.166 kg/s, plotting of bottom hole pressure vs time.

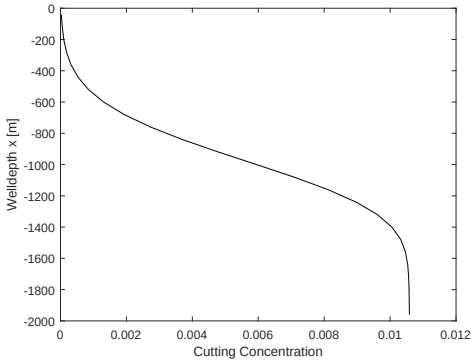

Figure 22: Case 4: t = 1500 s, mass rate = 0.498 kg/s, plotting of well depth vs cuttings concentration.

Case 5: In the present scenario, we discretize the well into 25 boxes and 50 boxes to examine the efficiency of proposed numerical scheme and effect of discretization on the

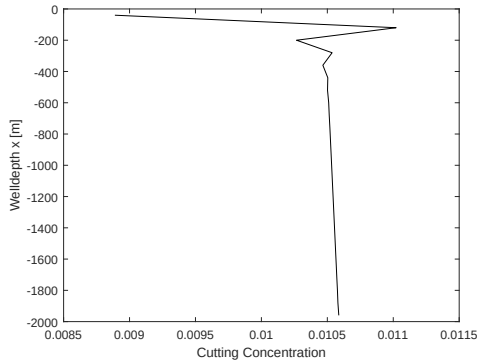

Figure 23: Case 4: t = 4000 s, mass rate = 0.498 kg/s, plotting of well depth vs cuttings concentration.

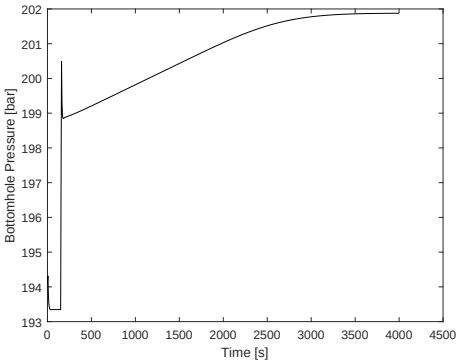

Figure 24: Case 4: t = 4000 s, mass rate = 0.498 kg/s, plotting of bottom hole pressure vs time.

two phase flows. Figure 25 displays the impact of increasing the number of boxes on the analysis. The transition zone between pure liquid and liquid/cuttings becomes sharper as the number of boxes increases. Clearly, steady state cutting concentration value becomes more precise with a finer grid (0.07 for 25 boxes vs 0.077 for 50 boxes). Thus, refining the grid brings us closer to the true value, which is 0.067. Figure 26 demonstrates that using 50 boxes results in less smearing of the cutting concentrations at 1500 s compared to 25 boxes. Similarly, in Figure 27, for 50 boxes and 2000 s, we observe a less smeared front. The steady state concentration values at the end differ between the two cases. Figure 28 shows steady state conditions at 3000 s, while in Figure 29, although we reach steady state, the cutting concentration values differ at 4000 s. Figure 30 illustrates the outlet rate, which is observed to be 24 kg/s initially. This is due to the pumping of liquids and cuttings from the bottom of the well. Nevertheless, the liquid flow rate diminishes to steady-state value of 22 kg/s, once the cuttings arrive at the outlet. Figure 31 displays the impact of numerical diffusion on the liquid mass rate. Initially, we observe a transit time of 2172 s for the cutting in the well. The simulation starts at 150 s. The transition is quicker and closer to the theoretical value when using 50 boxes compared to 25 boxes. A smooth curve showing a linear rise in the cutting mass rate is shown in Figure 32 from 2000 s to 2700 s. Four thousand seconds is the time required to achieve a steady state. Here, there is no difference between the cutting mass rate at the well's top and bottom. The impact of numerical diffusion becomes apparent once again when the cuttings reach the well's exit, when there is a rapid rise from 0 to 4 kg/s.

Figure 33 demonstrates the numerical diffusion effect. It is observed that by using 50 boxes the steady state attained more rapidly as compared to 25 boxes. It takes 3000 s to achieve the cutting mass rate associated with 50 boxes and 4 kg/s. This result is better when compared with the result of 25 boxes, takes 1000 s more. This result shows that the curve display a complete transition. Figure 34 shows the effect of numerical diffusion on BHP. We can observe an increase in BHP from $201 - 205$ bar at 200 s, which is due to friction. As the cuttings start to distribute in the well, there is a gradual build-up of pressure. The maximum BHP is 222 bar for the solid curve and 224 $bars$ for the dashed curve. When

the number of boxes is 50, we observe a difference of two bars in the maximum BHP value. This is because we obtain a more accurate cutting concentration value with 50 boxes. The proposed numerical scheme demonstrates improved efficiency and accuracy as the number of grid points increases, indicating good convergence behavior with mesh refinement.

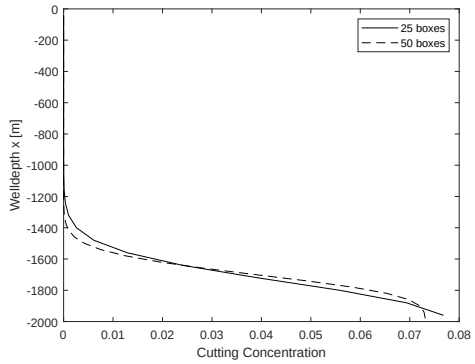

Figure 25: Case 5: t $= 500\ s$, mass rate $= 4\ kg/s$, plotting of well depth vs cuttings concentration.

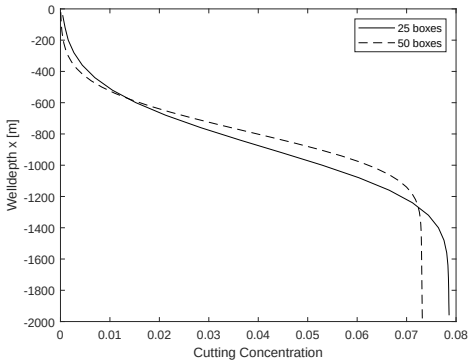

Figure 26: Case 5: t $= 1500\ s$,mass rate $= 4\ kg/s$, plotting of well depth vs cuttings concentration.

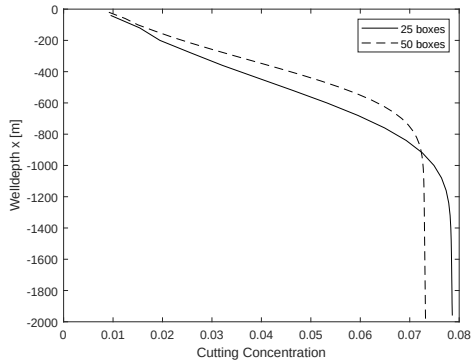

Figure 27: Case 5: t $= 2000\ s$, mass rate $= 4\ kg/s$, plotting of well depth vs cuttings concentration.

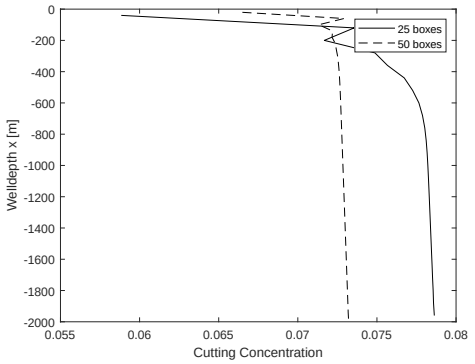

Figure 28: Case 5: t $= 3000\ s$, mass rate $= 4\ kg/s$, plotting of well depth vs cuttings concentration.

5. Conclusions

This study presented a high-order TVD Runge-Kutta Discontinuous Galerkin (RKDG) numerical scheme with WENO limiters to analyze the behavior of two-phase flow in drilling operations using the drift-flux model. The proposed method effectively handled the nonlinear nature of transport processes, accurately captured sharp interfaces, and suppressed non-physical oscillations near strong gradients. Through a series of test cases, a clear relationship was observed between increasing rate of penetration (ROP), cuttings concentration, and bottom hole pressure (BHP). These results demonstrate that the developed

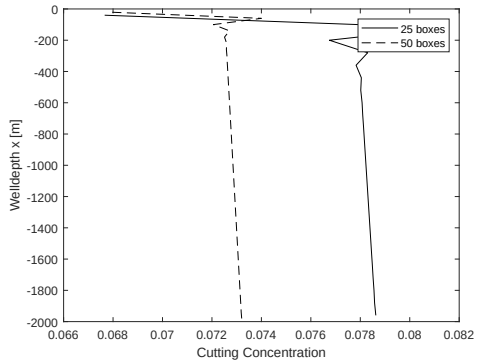

Figure 29: Case 5: t = 4000 s, mass rate = 4 kg/s, plotting of well depth vs cuttings concentration.

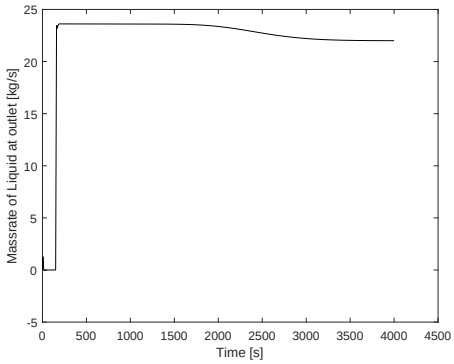

Figure 30: Case 5: t = 4000 s, mass rate = 4 kg/s, plotting of liquid mass rate out vs time.

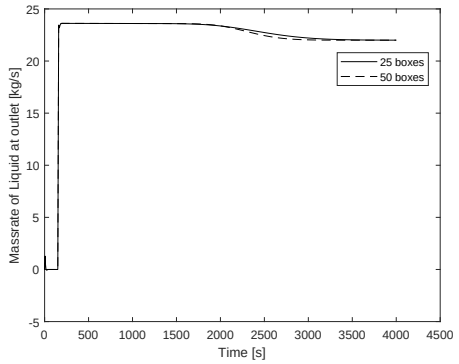

Figure 31: Case 5: t = 4000 s, mass rate = 4 kg/s, plotting of liquid mass rate out vs time.

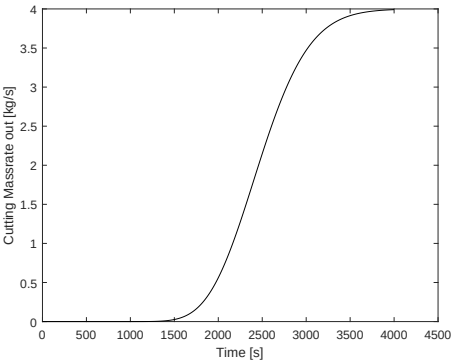

Figure 32: Case 5: t = 4000 s, mass rate = 4 kg/s, plotting of cuttings mass rate out vs time.

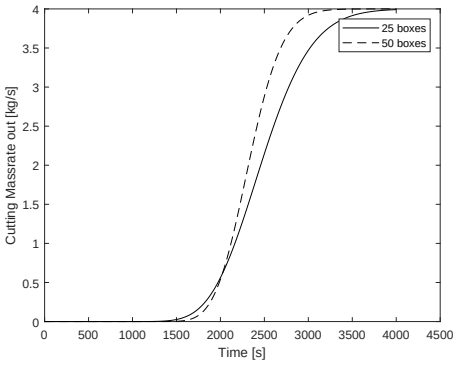

Figure 33: Case 5: t = 4000 s, mass rate = 4 kg/s, plotting of cuttings mass rate out vs time.

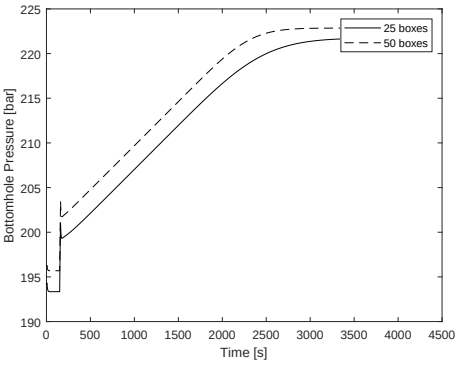

Figure 34: Case 5: t = 4000 s, mass rate = 4 kg/s, plotting of bottom hole pressure vs time.

scheme can provide reliable and accurate predictions for transient drilling hydraulics, offering an efficient tool for optimizing operational parameters. However, the current model

does not account for thermal effects or complex particle interactions like settling, agglomeration, or erosion. Future work can extend this study by incorporating more detailed two-fluid models, considering variable fluid properties, and including temperature-dependent behavior.

References

[1] P. H. Tomren, A. W. Lyoho, and J. J. Azar. Experimental study of cutting transport in directional wells. *SPE Drilling Engineering*, 1(01):43–56, 1986.

[2] R. A. Sanchez, J. J. Azar, A. A. Bassal, and A. L. Martins. The effect of drillpipe rotation on hole cleaning during directional well drilling. In *SPE/IADC Drilling Conference*. OnePetro, 1997.

[3] M. M. Huque, S. Butt, S. Zendehboudi, and S. Imtiaz. Systematic sensitivity analysis of cuttings transport in drilling operation using computational fluid dynamics approach. *Journal of Natural Gas Science and Engineering*, 81:103386, 2020.

[4] M. M. Huque, M. A. Rahman, S. Zendehboudi, S. Butt, and S. Imtiaz. Experimental and numerical study of cuttings transport in inclined drilling operations. *Journal of Petroleum Science and Engineering*, 208:109394, 2022.

[5] A. Zakerian, S. Sarafraz, A. Tabzar, N. Hemmati, and S. R. Shadizadeh. Numerical modeling and simulation of drilling cutting transport in horizontal wells. *Journal of Petroleum Exploration and Production Technology*, 8:455–474, 2018.

[6] M. Pelanti and R. J. LeVeque. High-resolution finite volume methods for dusty gas jets and plumes. *SIAM Journal on Scientific Computing*, 28(4):1335–1360, 2006.

[7] F. Dobran, A. Neri, and G. Macedonio. Numerical simulation of collapsing volcanic columns. *Journal of Geophysical Research: Solid Earth*, 98(B3):4231–4259, 1993.

[8] J. Dufek and G. W. Bergantz. Dynamics and deposits generated by the kos plateau tuff eruption: Controls of basal particle loss on pyroclastic flow transport. *Geochemistry, Geophysics, Geosystems*, 8(12), 2007.

[9] N. Zuber and J. A. Findlay. Average volumetric concentration in two-phase flow systems. *Journal of Heat Transfer*, 1965.

[10] J. E. Romate. An approximate riemann solver for a two-phase flow model with numerically given slip relation. *Computers & Fluids*, 27(4):455–477, 1998.

[11] K. K. Fjelde and K. H. Karlsen. High-resolution hybrid primitive–conservative upwind schemes for the drift flux model. *Computers & Fluids*, 31(3):335–367, 2002.

[12] E. Steinar and K. K. Fjelde. Hybrid flux-splitting schemes for a two-phase flow model. *Journal of Computational Physics*, 175:674–701, 2002.

[13] M. Baudin, C. Berthon, F. Coquel, R. Masson, and Q. H. Tran. A relaxation method for two-phase flow models with hydrodynamic closure law. *Numerische Mathematik*, 99:411–440, 2005.

[14] S. T. Munkejord, S. Evje, and T. Flåtten. The multi-stage centred-scheme approach applied to a drift-flux two-phase flow model. *International Journal for Numerical Methods in Fluids*, 52(6):679–705, 2006.

[15] J. L. Modisette and J. P. Modisette. Transient and succession-of-steady-states pipeline flow models. In *PSIG Annual Meeting*. OnePetro, 2001.

[16] W. H. Reed and T. R. Hill. Triangular mesh methods for the neutron transport equation. Technical Report LA-UR-73-479, Los Alamos Scientific Laboratory, 1973.

[17] J. S. Hesthaven and T. Warburton. *Nodal Discontinuous Galerkin Methods: Algorithms, Analysis, and Applications*, volume 54 of *Springer Texts in Applied Mathematics*. Springer, 2008.

[18] J. X. Qiu and C.-W. Shu. A numerical study for the performance of the runge-kutta discontinuous galerkin method based on different numerical fluxes. *Journal of Computational Physics*, 212:540–565, 2006.

[19] D. N. Arnold, F. Brezzi, B. Cockburn, and L. D. Marini. Unified analysis of discontinuous galerkin methods for elliptic problems. *SIAM Journal on Numerical Analysis*, 39:1749–1779, 2002.

[20] B. Cockburn and C.-W. Shu. Tvb runge-kutta local projection discontinuous galerkin finite element method for conservation laws ii: General framework. *Mathematics of Computation*, 52:411–435, 1989.

[21] B. Cockburn and S.-Y. Lin. Tvb runge–kutta local projection discontinuous galerkin finite element method for conservation laws iii: One-dimensional systems. *Journal of Computational Physics*, 84:90–113, 1989.

[22] B. Cockburn and C.-W. Shu. Runge–kutta discontinuous galerkin methods for convection-dominated problems. *Journal of Scientific Computing*, 1:173–261, 2001.

[23] B. Cockburn and C.-W. Shu. The runge–kutta local projection p^1-discontinuous galerkin method for scalar conservation laws. *Mathematical Modelling and Numerical Analysis*, 25:337–361, 1991.

[24] C.-W. Shu. Total-variation-diminishing time discretizations. *SIAM Journal on Scientific and Statistical Computing*, 9:1073–1084, 1988.

[25] C.-W. Shu and S. Osher. Efficient implementation of essentially non-oscillatory shock-capturing schemes. *Journal of Computational Physics*, 77:439–471, 1988.

[26] R. Y. Adrian et al. Numerical simulation on the behaviour of celular stainless-steel beam (cssb) at elevated temperature. *Journal of Engineering Sciences and Technology in Physics*, 19(1):25–39, 2024.

[27] B. AlHadeethi et al. Numerical modeling of flow pattern with different spillway locations. *Mathematical Modelling of Engineering Problems*, 11(5):1219–1226, 2024.

[28] M. A. Iqbal. Use of ausmv scheme for simulation of particle transport. M.sc. thesis, University of Stavanger, Norway, 2015.

[29] C.-W. Shu. Essentially non-oscillatory and weighted essentially non-oscillatory schemes for hyperbolic conservation laws. Technical Report NASA/CR-97-206253, ICASE Report No. 97-65, NASA ICASE, 1997.

[30] J. X. Qiu and C.-W. Shu. Runge–kutta discontinuous galerkin method using weno limiters. *Journal of Scientific Computing*, 26:907–929, 2005.

[31] X. Zhang and C.-W. Shu. On maximum-principle-satisfying high order schemes for scalar conservation laws. *Journal of Computational Physics*, 229:3091–3120, 2010.

[32] X. Zhang and C.-W. Shu. Positivity preserving high order discontinuous galerkin

schemes for compressible euler equations with source terms. *Journal of Computational Physics*, 230:1238–1248, 2011.

[33] E. A. Az-Zo'bi. On the reduced differential transform method and its application to the generalized burgers-huxley equation. *Applied Mathematical Sciences*, 8(177):8823–8831, 2014.

[34] E. A. Az-Zo'bi. A reliable analytic study for higher-dimensional telegraph equation. *Journal of Mathematics and Computer Science*, 18(4):423–429, 2018.

[35] E. A. Az-Zo'bi et al. Numeric-analytic solutions of mixed-type systems of balance laws. *Applied Mathematics and Computation*, 265:133–143, 2015.

[36] J. A. Haider et al. Results validation by using finite volume method for the blood flow with magnetohydrodynamics and hybrid nanofluids. *Modern Physics Letters B*, 38(24):2450208, 2024.

[37] K.K. Fjelde and K. H. Karlsen. High-resolution hybrid primitive-conservative upwind schemes for the drift-flux model. *Computers & Fluids*, 31(3):335–367, 2002.

[38] E. Steinar and K. K. Fjelde. Hybrid flux-splitting schemes for a two-phase flow model. *Journal of Computational Physics*, 175(2):674–701, 2002.

[39] C.-W. Shu. Tvb uniformly high-order schemes for conservation laws. *Mathematics of Computation*, 49(179):105–121, 1987.

[40] Gottlieb and C.-W. Shu. Total variation diminishing runge-kutta schemes. *Mathematics of Computation*, 67(221):73–85, 1998.